Modeling Microstructurally Small Fatigue Cracking Processes in an Aluminum Alloy with the PPR Cohesive Zone Model

Albert Cerrone[1], Gerd Heber[2], Paul Wawrzynek[1], Glaucio Paulino[3], Anthony Ingraffea[1]

Abstract: Most of total fatigue life in high strength aluminum alloy aerospace components is spent in microstructurally small stages of incubation, nucleation, and propagation (MSFC). Various interfaces are mobilized during these stages. Grain boundary decohesion and particle-matrix debonding are two of several such mobilizations in MSFC growth in granular materials, but due to inadequate constitutive models and lack of computational power, successfully modeling these debondings has been challenging. A new more robust cohesive zone model (CZM), the Park-Paulino-Roesler (PPR) potential-based CZM, is combined here with massively parallel nonlinear finite element analyses to accurately characterize these components of MSFC growth.

The first study examines grain boundary decohesion in idealized, cubical grain polycrystals. The second study investigates the nucleation of cracking within and from a second-phase particle. In previous studies, all particle-grain and grain-grain interfaces were assumed perfectly bonded. The inclusion of cohesive elements along these interfaces offers new insights into MSFC life around a second-phase particle, and computationally, how tractable this methodology is for larger, more comprehensive studies. The overarching impetus for this work is to add to the body of knowledge of MSFC stages of total life, contributing to the development of a technique that translates observations made at the microscale to the componentscale.

Introduction

A grain boundary is an interface between two grains, or a transition zone from one crystallographic orientation to another. The grains in an AA7075-T651 rolled sheet microstructure are elongated or pancake-shaped, and ductile crack growth in this alloy is predominately initiated by void coalescence formed at second-phase particles. Further, in this alloy, a major source for fatigue crack incubation is the brittle fracture of Al_7Cu_2Fe second phase particles. As Grosskreutz and Shaw (1969) observed in a 2000-series aluminum alloy, debonding between the particle and matrix occurs in tandem with brittle crack nucleation of the particle. Aluminum alloy grain-particle debonding was modeled in two-dimensions by Gall *et al.* (2001) and Dodhia (2002), but more advanced investigations of the mechanics governing MSFC life in AA7075-T651 (Bozek *et al.* 2008; Hochhalter *et al.* 2010; Veilleux 2011) did not model this decohesion. Intergranular fracture, crack growth along a grain boundary, is also prevalent in some alloys and is caused by mechanisms including intergranular corrosion, brittle phase deposition on a grain boundary, environmental cracking, and high-temperature intergranular cavitation (Anderson 2005). Grain boundary decohesion has been studied using computer simulations, and the level of complexity has increased from the very basic two-dimensional models of Raj and Ashby (1975) to Iesulauro's (2006) ten-million degree-of-freedom (DOF) three-dimensional finite element analyses. The three-dimensional nonlinear finite element analyses described herein attempt to model accurately both grain-particle debonding and intergranular fracture.

A current major obstacle to modeling decohesion in polycrystals is the lack of a robust CZM well-suited for mixed-mode fracture. Three-dimensional polycrystal analyses are highly nonlinear and, depending upon the underlying constitutive laws and model geometry, tend to be mixed-mode. The finite element analyses discussed in this paper demonstrate the efficacy of the Park-Paulino-Roesler (PPR) potential-based cohesive zone model (CZM) (Park *et al.* 2009) in modeling decohesion amidst this nonlinearity and mode-mixity. The PPR CZM acts as the criterion for the nucleation of cracks. Nucleation occurs when the cohesive elements discretizing an interface incur a normal or shear traction greater than the specified cohesive strengths. Decohesion continues until a critical separation is reached, or, equivalently, until the cohesive elements dissipate predefined fracture energies. At this point the nucleated crack is called a true crack that is incapable of transferring normal or shear stress. The hallmark of the PPR CZM for the purposes of modeling decohesion is its ability to handle high degrees of mode-mixity; it allows a set of failure responses and allows the researcher to specify independent normal and shear cohesive strengths and fracture energies.

Two types of finite element models were analyzed in this study. The first, denoted Type I, was an idealized cubical polycrystal consisting of cubical grains and no second-phase particles loaded uniaxially in simple tension. The second, denoted Type II, was an idealized cubical grain with an embedded semi-elliptical particle in one of the grain's faces, Figure 1. The massively parallel analyses were conducted on supercomputers using a nonlinear finite element solver built on a robust parallel architecture. The following methodology section serves to lay out the details of the analyses: FEM model specifics, parameters of the constitutive models, and computational effort are

[1] Cornell Fracture Group, Cornell University, Ithaca, NY 14853, USA
[2] The HDF Group, Champaign, IL 61820, USA
[3] Department of Civil and Environmental Engineering, University of Illinois at Urbana-Champaign, Urbana, IL 61801, USA

discussed in detail. Observations and conclusions follow.

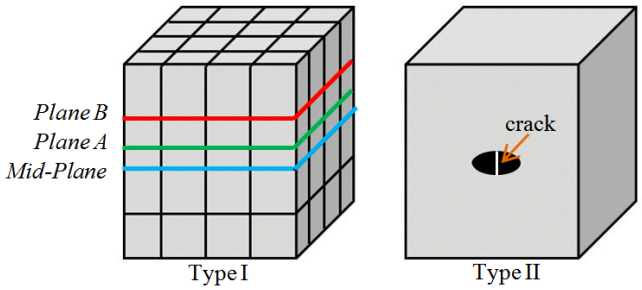

Figure 1: Type I and Type II FE models.

Methodology

Material Models

The linear-elastic, isotropic (LEI) material properties of the AA7075-T651 grains are given in Table 1 and were used primarily for verification purposes. An elasto-viscoplastic, rate-dependent FCC crystal plasticity constitutive model was employed (Matouš and Maniatty 2004) to account for the crystalline lattice structure of the grains. This model's parameters are given in Table 2. See Appendix I for a brief description of these parameters or Bozek *et al.* (2008) for a more comprehensive explanation.

Table 1: LEI grain material properties.

E	**ν**
72GPa	0.33

Table 2: Rate-dependent FCC crystal plasticity material parameters.

m	**g_o**	**$\dot{\gamma}_o$**	**G_o**	**g_s**	**# Slip Systems**
0.005	220MPa	$1.0s^{-1}$	120MPa	250MPa	12

μ	**λ**	**η**	**$\varphi_1, \Phi, \varphi_2$**
28,300MPa	60,900MPa	5,100MPa	$\varphi_1, \Phi, \varphi_2$

Cohesive zone models describe the grain boundary response. Iesulauro (2006) determined that the numerical stability of analyses on polycrystals with cohesive elements discretized along the grain boundaries is highly dependent upon the CZM. Employing a bilinear coupled CZM developed by Tvergaard and Hutchinson (1992), "coupled" meaning that the normal and tangential tractions and displacements are coupled into single measures, Iesulauro observed locking in several analyses. Locking is a purely numerical phenomenon that occurs when the finite element model is unable to accommodate additional deformation due to an insufficient number of paths for load distribution. For example, one situation that engenders locking is when a soft grain is pinned between stiffer grains. The soft grain wants to stretch; however, because the stiff grains cannot accommodate this additional deformation, the model locks in its current state. Despite varying grain geometry, polycrystal size, and constitutive model parameters, Iesulauro could not identify a method to circumvent locking. The underlying coupled CZM was to blame. In a highly mixed-mode analysis, if a cohesive element fails in mode-II, then by Tvergaard's and Hutchinson's CZM, it loses its ability to transmit traction in mode-I. The inverse is true, as well. Had a CZM adept in mixed-mode fracture with uncoupled measures of traction and displacement been implemented, the premature failure of cohesive elements would have been avoided, preserving an adequate number of paths for load distribution and circumventing locking.

The PPR is one such CZM. This potential-based CZM overcomes some limitations of previous potential-based models (Needleman 1987; Needleman 1990; Xu and Needleman 1993) such as ill-defined fracture parameters, large artificial compliance, and infinite final crack opening width. The PPR potential is given in Equation 1, a function of energy constants Γ_n and Γ_t, fracture energies ϕ_n and ϕ_t, non-dimensional exponents m and n, shape parameters α and β, final crack opening widths δ_n and δ_t, and cohesive separations Δ_n and Δ_t.

$$\Psi(\Delta_n,\Delta_t)=min(\phi_n,\phi_t)+\left[\Gamma_n\left(1-\frac{\Delta_n}{\delta_n}\right)^{\alpha}\left(\frac{m}{\alpha}+\frac{\Delta_n}{\delta_n}\right)^{m}+\langle\phi_n-\phi_t\rangle\right]\ldots$$
$$\ldots\left[\boldsymbol{\Gamma_t}\left(\mathbf{1}-\frac{|\Delta_t|}{\boldsymbol{\delta_t}}\right)^{\boldsymbol{\beta}}\left(\frac{\boldsymbol{n}}{\boldsymbol{\beta}}+\frac{|\Delta_t|}{\boldsymbol{\delta_t}}\right)^{\boldsymbol{n}}+\langle\boldsymbol{\phi_t}-\boldsymbol{\phi_n}\rangle\right] \quad (\mathbf{1})$$

Expressions for the energy constants Γ_n and Γ_t are given in Equation 2:

$$\Gamma_n=(-\phi_n)^{\frac{\langle\phi_n-\phi_t\rangle}{\phi_n-\phi_t}}\left(\frac{\alpha}{m}\right)^{m}\quad,\quad \Gamma_t=(-\phi_t)^{\frac{\langle\phi_t-\phi_n\rangle}{\phi_t-\phi_n}}\left(\frac{\beta}{n}\right)^{n}\quad for\ \phi_t\neq\phi_n \qquad (2)$$
$$\Gamma_n=-\phi_n\left(\frac{\alpha}{m}\right)^{m}\quad,\quad \Gamma_t=\left(\frac{\beta}{n}\right)^{n}\quad for\ \phi_t=\phi_n$$

The non-dimensional exponents m and n in Equation 3 are functions of the shape parameters and initial slope indicators λ_n and λ_t given in Equation 4:

$$m=\frac{\alpha(\alpha-1)\lambda_n^2}{1-\alpha\lambda_n^2}\quad,\quad n=\frac{\beta(\beta-1)\lambda_t^2}{1-\beta\lambda_t^2} \qquad (3)$$
$$\lambda_n=\frac{\delta_{nc}}{\delta_n}\quad,\quad \lambda_t=\frac{\delta_{tc}}{\delta_t} \qquad (4)$$

The initial slope indicators are measures of cohesive stiffness and control cohesive elastic behavior. Smaller initial slope indicators engender higher cohesive stiffness, which in turn decreases artificial elastic deformation. They are functions of δ_{nc} and δ_{tc}, the normal and tangential crack opening widths, respectively, corresponding to maximum normal and tangential cohesive strength and δ_n and δ_t, normal and tangential final crack opening widths, respectively, given by the expressions in Equation 5:

$$\delta_n=\frac{\phi_n}{\sigma_{max}}\alpha\lambda_n(1-\lambda_n)^{\alpha-1}\left(\frac{\alpha}{m}+1\right)\left(\frac{\alpha}{m}\lambda_n+1\right)^{m-1} \qquad (5)$$
$$\delta_t=\frac{\phi_t}{\tau_{max}}\beta\lambda_t(1-\lambda_t)^{\beta-1}\left(\frac{\beta}{n}+1\right)\left(\frac{\beta}{n}\lambda_t+1\right)^{n-1}$$

Taking the gradient of the potential Ψ yields the normal and tangential cohesive stresses T_n and T_t, respectively. Their expressions are given in Equation 6 and are plotted in Figure 2.

$$T_n(\Delta_n,\Delta_t)=\frac{\Gamma_n}{\delta_n}\left[m\left(1-\frac{\Delta_n}{\delta_n}\right)^{\alpha}\left(\frac{m}{\alpha}+\frac{\Delta_n}{\delta_n}\right)^{m-1}-\alpha\left(1-\frac{\Delta_n}{\delta_n}\right)^{\alpha-1}\left(\frac{m}{\alpha}+\frac{\Delta_n}{\delta_n}\right)^{m}\right]\ldots$$
$$\ldots\left[\Gamma_t\left(1-\frac{|\Delta_t|}{\delta_t}\right)^{\beta}\left(\frac{n}{\beta}+\frac{|\Delta_t|}{\delta_t}\right)^{n}+\langle\phi_t-\phi_n\rangle\right]$$
$$T_t(\Delta_n,\Delta_t)=\frac{\Gamma_t}{\delta_t}\left[n\left(1-\frac{|\Delta_t|}{\delta_t}\right)^{\beta}\left(\frac{n}{\beta}+\frac{|\Delta_t|}{\delta_t}\right)^{n-1}-\beta\left(1-\frac{|\Delta_t|}{\delta_t}\right)^{\beta-1}\left(\frac{n}{\beta}+\frac{|\Delta_t|}{\delta_t}\right)^{n}\right]\ldots \qquad (6)$$
$$\ldots\left[\Gamma_n\left(1-\frac{\Delta_n}{\delta_n}\right)^{\alpha}\left(\frac{m}{\alpha}+\frac{\Delta_n}{\delta_n}\right)^{m}+\langle\phi_n-\phi_t\rangle\right]\frac{\Delta_t}{|\Delta_t|}$$

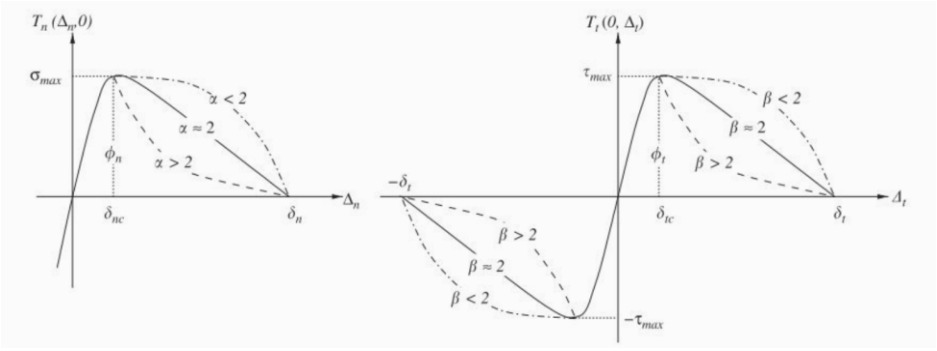

Figure 2: Cohesive fracture envelopes for PPR CZM [adapted from Park *et al.* (2009)].

The PPR-equivalent cohesive parameters that Iesulauro employed to model grain boundary decohesion in aluminum alloys are given in Table 3. They were employed here for PPR implementation verification purposes.

The verification model consisted of three elements: two 1mm-cubic bulk LEI elements and one zero-thickness cohesive element placed between them. The system was loaded in tension until cohesive failure. The bulk elements were assigned a Young's modulus one-hundred-times that of AA7075-T651, permitting very little bulk deformation. Consequently, the global response nearly mimicked the traction-separation law defined by the PPR parameters. The stress in the loading direction was uniform throughout the model and is plotted in Figure 3 versus displacement at the nodes assigned the nonzero essential boundary conditions. From Equation 5, the final crack opening width is evaluated to be 0.005mm, and the global response plot confirms this. Moreover, linear softening is observed (which was enforced by setting $\alpha = \beta = 2$), the maximum stress corresponds to the 450MPa cohesive strength, and the area under the curve is equivalent to the assigned fracture energy.

Table 3: Validation PPR parameters.

σ_{max}, τ_{max}	ϕ_n, ϕ_t	λ_n, λ_t	α, β
450MPa	1.125MPa-mm	0.005	2

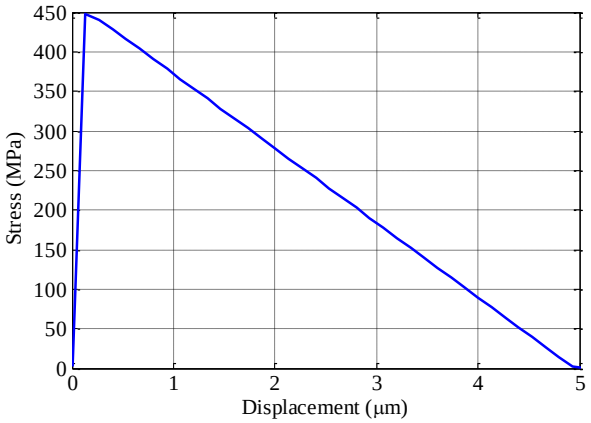

Figure 3: PPR Verification Model; stress in loading direction versus displacement in loading direction.

To gauge the PPR's efficacy in circumventing locking in a highly mixed-mode analysis, a 64 irregularly-shaped grain polycrystal loaded in simple tension was considered. The undeformed and final deformed polycrystals are visualized in Figure 4. For simplicity, the grains were assigned the LEI material properties given in Table 1 and were discretized by 230,471 quadratic tetrahedral elements. The grain boundaries were discretized by 19,472 zero-volume quadratic cohesive elements. Two CZMs were considered: the PPR and Tvergaard's and Hutchinson's coupled CZM (Iesulauro's coupled CZM parameters and the PPR-equivalent parameters given in Table 3 were used here). Two analyses were run, each with one of the CZMs considered, with identical linear and nonlinear solver options. Prior to softening in both analyses, convergence was reached in very few Newton iterations. The number of Newton iterations per load step increased by a factor of three in both analyses at the onset of global softening. During softening, the PPR analysis' convergence rate remained steady with relatively low converged residual norms. The coupled CZM analysis, on the other hand, struggled to reach acceptably converged states of equilibrium during softening--- the converged residual norms were on the order of 1E-2, approximately two orders of magnitude larger than the PPR's. If strict tolerances would have been set, the coupled CZM analysis would have locked and terminated shortly after onset of global softening.

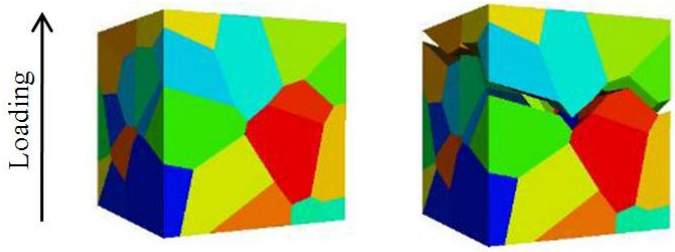

Figure 4: Undeformed and deformed 64-grain polycrystal.

Type I Model: Grain Boundary Decohesion

Finite Element Model Geometry and Boundary Conditions:

The Type I finite element models were composed of sixty-four grains. Iesulauro determined that for idealized cubical-grain polycrystals with cohesive grain boundaries, the 64-cube polycrystal is a representative volume element (RVE) by demonstrating the consistency of its global response in spite of variation in internal properties at the length scale shown in Figure 5. The grains were 0.05mm cubes. The polycrystals were loaded in simple tension with a 3-percent applied strain, Figure 5.

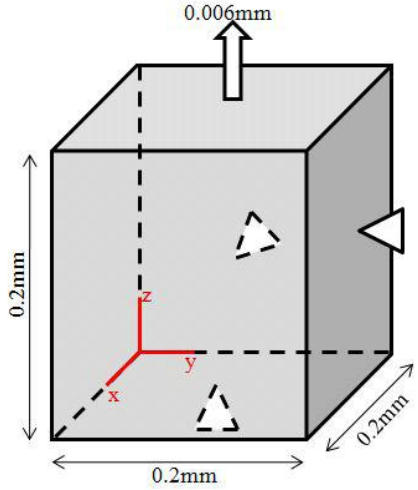

Figure 5: Type I FE Model; simple tension boundary condition.

The finite element meshes were generated in ABAQUS, post-processed in MATLAB for cohesive element insertion, and subsequently analyzed using the nonlinear finite element solver Finite Element All-Wheel Drive (FEAWD). FEAWD is built partially on PETSc, a suite of parallel routines including adaptive and fixed stepping algorithms and linear and nonlinear solvers (Balay *et al.* 1997, 2010, 2011).

Mesh Density Considerations:

This issue was first addressed by considering the cohesive zone length of AA7075-T651. An estimate for cohesive zone size for Dugdale-type CZMs in plane strain is given in Equation 7 (Rice 1968).

$$\Delta_{cohesive} = \frac{\pi E \phi_n}{8(1-\nu^2)\sigma_{max}^2} \qquad (7)$$

Equation 7 is a plastic zone size estimate that informs how dense the cohesive discretization should be. If this discretization were too coarse, meaning that an inadequate number of cohesive elements were to span any grain edge, the cohesive traction distributions would be erroneously resolved. For this alloy, E = 72,000MPa, mode-I fracture energy ϕ_n = 1.125N/mm, ν = 0.33, and σ_{max} = 450MPa. These values yield a cohesive zone length of about 0.18mm. This nonrestrictive bound on element size did not warrant the use of extremely coarse finite element meshes. Though the cubical grain geometry may have been easily represented with relatively few elements, the rate-dependent crystal plasticity constitutive model requires a refined mesh. Consequently, it was critical that mesh refinement studies be carried out to determine a converged finite element mesh.

Four meshes of varying refinement levels were considered. Their particulars are given in Table 4. 10-noded quadratic order tetrahedral bulk elements and 12-noded zero-volume cohesive elements composed each mesh. The grains were assigned the rate-dependent crystal plasticity parameters given in Table 2 with randomized grain orientations. The grain boundaries, in turn, were assigned the PPR parameters given in Table 3 except for those on the mid-plane perpendicular to loading, Figure 1. These were assigned a 2% reduction in cohesive strength. Convergence was studied on two levels: global and local. The global level referred solely to the load-displacement response of the polycrystal. Referring to Figure 6, a plot of the polycrystal's cumulative load versus applied displacement, the extremely coarse Mesh 1 and the refined Mesh 4 yielded virtually identical results, suggesting that a strict upper bound on element size was not required to accurately resolve the polycrystal's global response.

Table 4: Type I Models: Cubical grain polycrystal meshes.

Mesh ID	# of Bulk Elements	# of Cohesive Elements	# of DOF
1	4,056	1,152	27,840
2	15,494	2,856	88,386
3	129,900	11,232	615,642
4	504,482	32,022	2,283,576

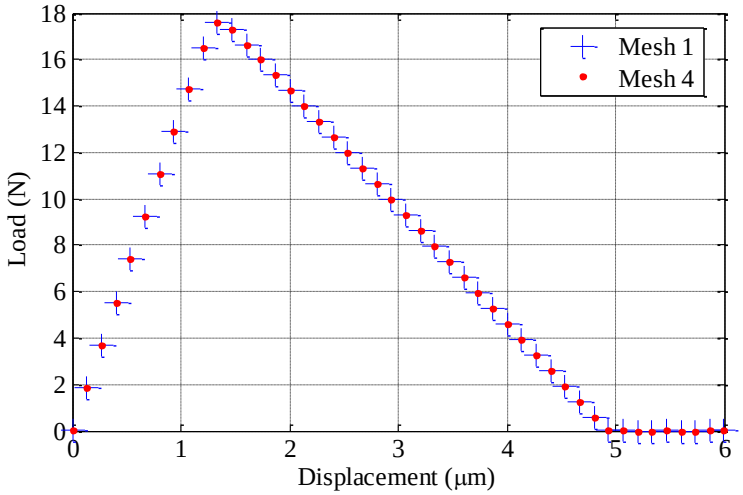

Figure 6: Converged global response data.

With regards to a local mesh convergence study, a mesh was said to be adequately refined if Gauss-point level data between successive meshes were acceptably similar. A structured grid composed of 1,331 grid points was fitted to each mesh and material-specific stresses, sigma_z, were subsequently mapped to each grid point. For this refinement study, two sampling regions were chosen: a plane bisecting cohesive planes perpendicular to loading, Plane A in Figure 1, and a cohesive plane perpendicular to loading, Plane B. Stresses from Meshes 1-3 were compared against stresses from Mesh 4, and the data are given in Tables 5 and 6. As expected, Mesh 1 yielded the worst agreement of the three, especially in the cohesive plane region prior to global softening. Mesh 2 was a marked improvement while Mesh 3, the densest of the three meshes, yielded the best agreement particularly away from cohesive planes. Convergence in a local stress measure was evident.

Table 5: Mean of percent difference in sigma_z on Plane A.

Mesh ID	Prior to Global Softening	Initiation of Softening	Post Softening
1-4	0.42	0.41	0.44
2-4	0.18	0.18	0.20
3-4	0.041	0.037	0.041

Table 6: Mean of percent difference in sigma_z on Plane B.

Mesh ID	Prior to Global Softening	Initiation of Softening	Post Softening
1-4	1.44	0.75	0.76
2-4	0.99	0.51	0.51
3-4	0.37	0.31	0.30

Slip was also considered in the local mesh convergence study. As expected, Figure 7 shows that the location and magnitude of slip was more accurately captured for increasing mesh refinement. Meshes 1 and 2 did a relatively good job characterizing the location of slip, but the magnitude was underestimated in some regions. Mesh 3 did an adequate job on both fronts.

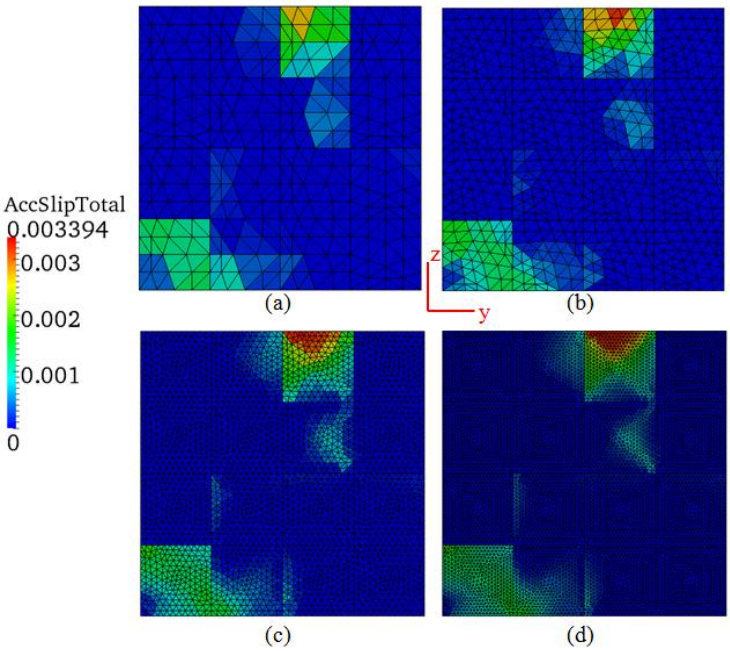

Figure 7: Total accumulated plastic slip for meshes 1-4, a-d, respectively.

Taking into consideration the results of both convergence studies, the refinement level of Mesh 3 offered the most acceptable tradeoff between efficiency and accuracy. The Type I FE analyses mentioned later in this paper contained a discretized solution space with Mesh 3's level of refinement.

Computational Resources and Solver Specifics:
The Type I FE analyses were conducted on the Cornell Fracture Group's ADMMII cluster. This machine is comprised of thirty-two nodes, each with two 2.5 GHz Intel Xeon quad-core processors. The computational resources utilized for each mesh along with approximate wall clock times are given in Table 7. For all analyses, a Newton method with trust region nonlinear solver was used along with a biconjugate gradient Krylov subspace method and a Jacobi preconditioner. It is noteworthy that a Newton method with cubic line search did not converge upon the onset of cohesive softening, and therefore a trust region method was employed with its strong global and local convergence properties. The 3% strain was applied in 9,000 load steps with a fixed stepping scheme.

Table 7: Type I FE model computational resources and effort.

Analysis	**# of Nodes**	**# of Cores**	**Approx. Wall Clock Time (days)**
Mesh 1	1	4	1
Mesh 2	1	4	2
Mesh 3	6	24	7
Mesh 4	16	96	42

Type II Model: Particle-Matrix Debonding

Finite Element Model Geometry and Boundary Conditions:
The Type II finite element model was adapted from Hochhalter's (2010) studies with perfectly bonded particle-matrix interfaces. The model emulates a grain containing a second-phase particle positioned at the surface of a notch of a double edge-notched specimen. Verification of this model was conducted by Bozek *et al.* (2008) and was composed of one cubical region representing a grain and a semi-elliptical region representing the particle. This particle protruded into the grain from the surface that was perpendicular to the transverse direction (TD). Moreover, the particle was nucleated or cracked along its mid-plane normal to the rolling direction (RD). See Figure 8 for details. The model's boundary conditions are also given in Figure 8. The semi-elliptical particle had a 2.0μm major axis and 1.0μm minor axis on surface, and a 1.0μm semi-minor axis in the TD.

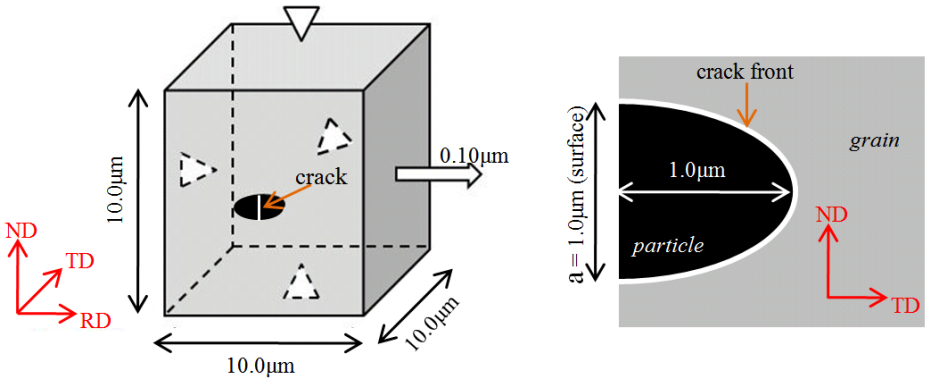

Figure 8: Type II FE Model: dimensions, boundary conditions, and particle mid-plane cross-section.

Mesh Density Considerations:
Zero-volume cohesive elements were inserted along the grain-particle interface. They were assigned the PPR parameters given in Table 3. The bulk elements discretizing the particle were quadratic tetrahedra modeled as LEI with E = 166.4GPa (approximately twice that of the average grain stiffness) and ν = 0.30. As in the Type I FE models, the hybrid quadratic tetrahedral elements discretizing the grain were assigned the rate-dependent crystal plasticity parameters given in Table 2. A "low stress" grain orientation adapted from Bozek *et al.* (2008) was considered. With regards to mesh refinement, it was crucial that an adequate number of elements discretize the nucleated crack front in order to capture the localization there. This requirement was far more stringent than the cohesive zone length given by Equation 7 and the element size restrictions stemming from the crystal plasticity model explored previously for the Type I FE model. Hochhalter investigated four different mesh refinement levels ranging from 150,000 DOF to 2.5-mil DOF, and tested convergence on nucleation metrics calculated along a non-local arc radius. The FE mesh used here, Hochhalter's concentrated refinement mesh with cohesive elements, required 2,669,526 equations to be solved iteratively per load step.

Computational Resources and Solver Specifics:
The presence of three different material models in the immediate vicinity of the crack front, along with its highly refined mesh, made the Type II FE model computationally expensive. Unlike Mesh 4 of the Type I FE model, the grain-particle mesh necessitated relatively high nonlinear solver solution-times due primarily to the analysis' high degree of mode-mixity from several thousand different cohesive element orientations. A supercomputer capable of exploiting FEAWD's ability to scale to several hundred cores was required. Consequently, the analysis was run on 256 cores. A fixed stepping scheme and the same solver options from the Type I FE model were implemented here.

Observations

Type I Model

The majority of cohesive elements on the weakened mid-plane began to soften at approximately 22% of the applied 3% strain. Recall from Table 2 that the initial slip resistance or critical resolved shear stress of AA7075-T651 is 220MPa. Prior to global softening, only one of the grains exhibited slip. Just after the initiation of softening, the resolved shear stress on several slip planes clearly rose above the critical value, Figure 9. For demonstration purposes, the initial slip resistance was lowered to 200MPa in Figure 10. Prior to the majority of cohesive elements on the weakened mid-plane softening, slip was minimal. Just after the initiation of cohesive softening, the total accumulated slip sharply rose throughout the polycrystal, with the highest degrees of slip occurring around the vicinity of the weakened mid-plane. It is noteworthy that only a 9% reduction in critical resolved shear stress caused increases in total accumulated slip by factors as high as thirty-five in some regions of the model.

To further highlight the interplay between cohesive softening and slip, another analysis was run. This time, the cohesive strengths, as opposed to the critical resolved shear stress, were modified to allow for a higher degree of plastic slip prior to the onset of cohesive softening. The cohesive strengths used in the previous analyses were increased by 10% while the grain properties given in Table 2 were employed with no modification to the initial slip

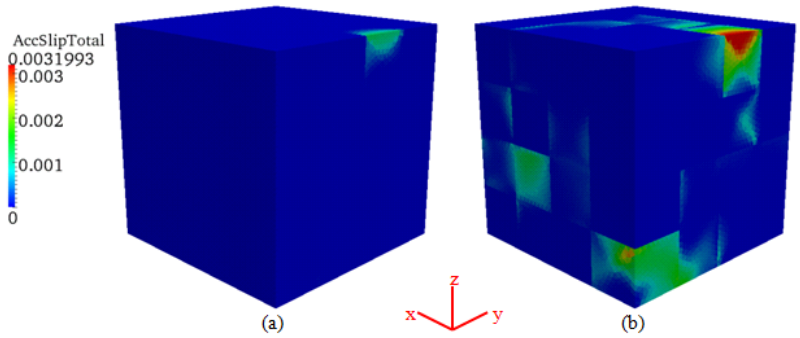

Figure 9: Accumulated total plastic slip prior to (a) and just after initiation (b) of global softening for g_o = 220MPa.

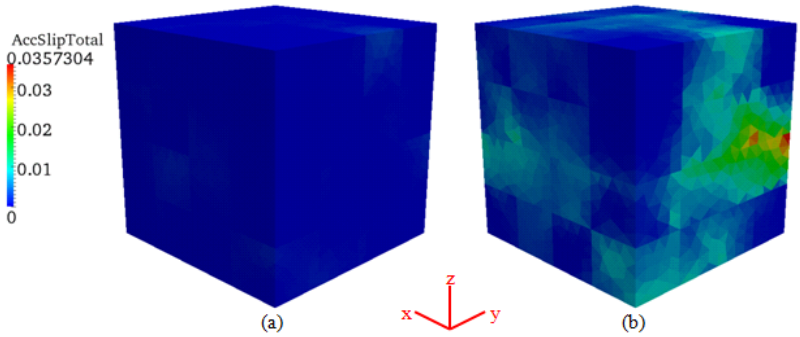

Figure 10: Accumulated total plastic slip prior to (a) and just after initiation (b) of global softening for g_o = 200MPa.

resistance parameter. Figure 11 shows that the 10% increase in cohesive strength allowed for a much greater occurrence of slip. The effect is similar to the previous case; however, significantly more slip planes were activated prior to the initiation of global softening. Nevertheless, the prevalence and magnitude of total accumulated slip rose considerably just after the initiation of softening.

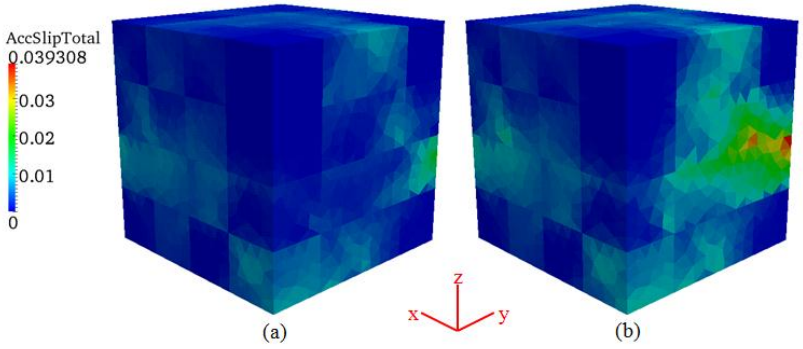

Figure 11: Accumulated total slip prior to (a) and just after initiation (b) of global softening for increased cohesive strength.

Type II Model

The nonlinear solver performed well up to 25% of the applied 1% strain. In order to ensure nonlinear solver convergence after this stage, smaller load steps were needed; increments as low as 0.0010% of the applied 0.10μm displacement were taken towards the end of the analysis. It is noteworthy that the Type I analyses did not suffer from these stringent stepping requirements. Due in part to the variability in cohesive element orientation, the confluence of three different material models at the crack front, the required highly refined mesh, and the relatively high stress gradients around the crack front, the Type II analysis was significantly more computationally expensive and susceptible to solver divergence than its Type I counterparts.

Particle-matrix debonding was observed. Figure 12 shows debonding at 100% of the applied 1% strain occurred where the crack front daylights onto the free surface (a) and at the ends of the particle's major axis (b). Occurrences of complete debonding were localized in these specific regions and did not extend to any appreciable degree in the TD. This did not suggest that the majority of cohesive elements had not softened, just that a relative few had lost their ability to transmit stress. In fact, the presence of debonding through the cohesive elements had noticeably affected the amount of slip around the particle.

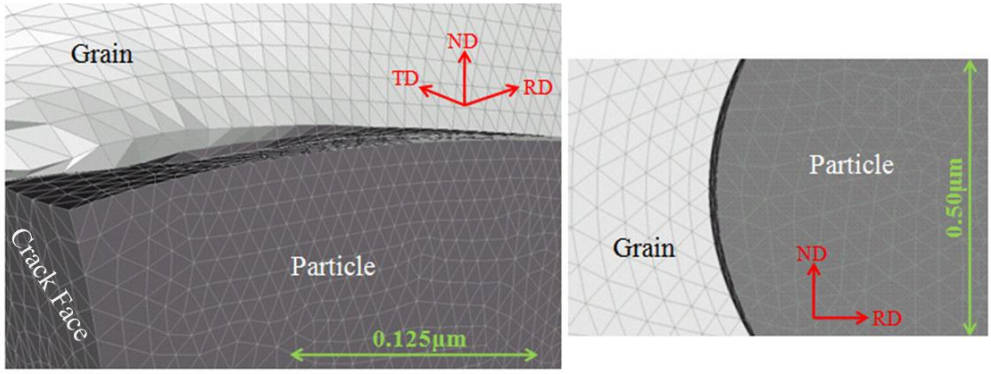

(a) (b)

Figure 12: Particle-matrix debonding where the crack front daylights onto free surface (a) and at an end of the particle's major axis on surface (b).

To demonstrate the debonding impact upon the stress state around the particle, three damage metrics calculated from Hochhalter's non-cohesive analysis and the analysis discussed here were considered. The damage metrics were sampled at 100% of the 1% applied strain along an arc with radius of 25% of the crack dimension 1.0μm (*a* in Figure 8), and drawn from a node on the crack front, Figure 13. The arc radius was determined by Hochhalter and corresponds to the minimum distance from the crack front at which the nucleation metrics are not dominated by the crack. D_1, the first damage metric, is the maximum value of slip rate over the twelve slip systems. D_2 is the maximum value of total accumulated slip over each slip plane and D_3 is the total accumulated slip over all twelve slip systems. These three metrics are plotted in Figure 14. For all three damage metrics, local debonding through cohesive elements had the effect of raising each considerably along the majority of the sampling arc. To quantify this increase, both the maximum and mean values of D_1, D_2, and D_3 along the non-local arc were considered. These are given in Tables 8 and 9. The maximum values suggest approximately a 62% increase for the three metrics. The mean values, on the other hand, suggest increases ranging from 85-92%. Intuitively, this increase is to be expected. As cohesive elements soften and, in some cases, fail, the resolved shear stresses around the particle increase. Consequently, the magnitude of slip over each slip plane increases. This same phenomenon was observed in the Type I analyses just after the initiation of global softening.

Conclusions

Modeling both intergranular fracture and particle-matrix debonding are computationally intensive tasks. The PPR CZM, amidst the high degrees of mode-mixity and nonlinearity in both sets of analyses, resolved decohesion and debonding without numerical difficulties such as locking. The Type I FE model investigation demonstrated certain mesh refinement requirements for a crystal plastic – cohesive polycrystal and the interplay between cohesive softening and slip. Of particular importance is the observation that the prevalence and magnitude of slip throughout the polycrystal increased by a significant amount just after the initiation of global softening. The Type II FE model

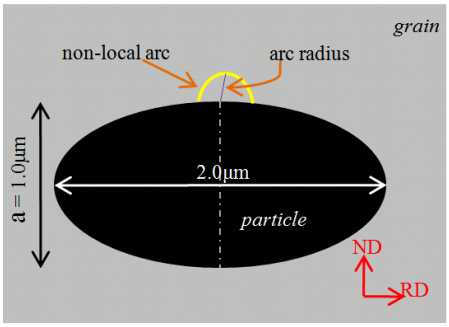

Figure 13: Non-local arc radius drawn from a crack front node on the free surface.

investigation, the more complex of the two, has proven that a FE model with various cohesive element orientations and a crack front in the immediate vicinity of three different material models is computationally feasible. The load step size must be limited to ensure convergence, but the analysis is nevertheless tractable assuming access to 200+ cores is available for models with a few million DOF. Moreover, the investigation has shown that the inclusion of cohesive elements to model grain-particle debonding, as opposed to assuming a perfectly bonded condition, produces a significant difference in the stress state around the particle, particularly with regards to resolved shear stress.

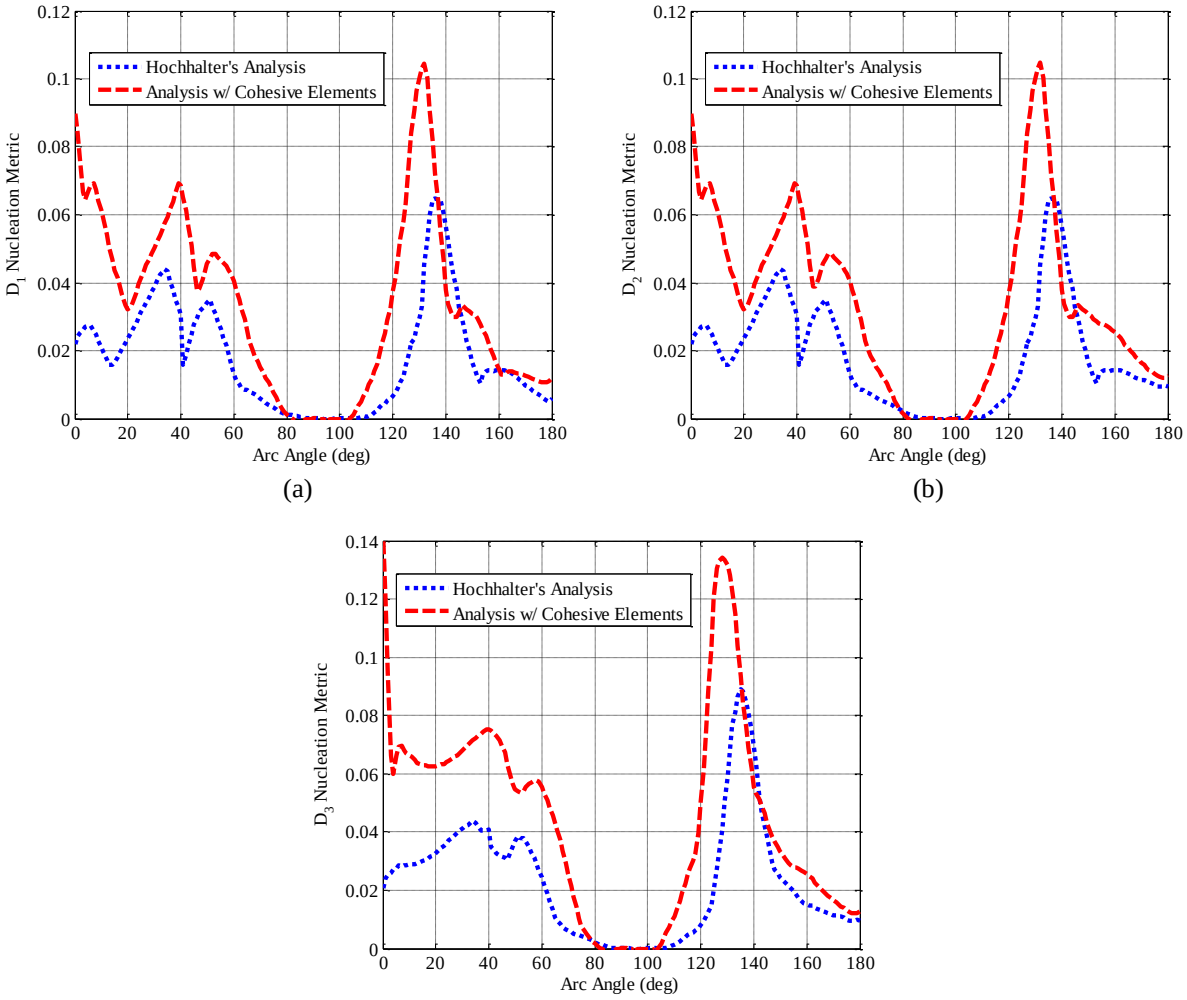

(a) (b)

(c)

Figure 14: Plots of D_1, D_2, and D_3, a, b, and c, respectively, along an arc with radius of 25% of the crack dimension 1.0μm at 100% of the applied 1% strain.

Table 8: Maximum nucleation metric along non-local arc.

Metric	Non-Cohesive Analysis	Cohesive Analysis	% Increase
D_1	0.0647	0.1046	61.7
D_2	0.0647	0.1047	61.8
D_3	0.0892	0.1437	61.1

Table 9: Average nucleation metric along non-local arc.

Metric	Non-Cohesive Analysis	Cohesive Analysis	% Increase
D_1	0.0179	0.0332	85.5
D_2	0.0182	0.0340	86.8
D_3	0.0230	0.0442	92.2

Acknowledgements

The authors of this paper would like to recognize the generous contributions to this research of former Cornell Fracture Group members Michael Veilleux, PhD, and Jacob Hochhalter, PhD. Their experience with FEAWD and visualizing FE microstructures was invaluable.

Appendix I: List of Symbols

Cohesive Parameters

ϕ_n, ϕ_t	mode-I and mode-II fracture energies
Δ_n, Δ_t	normal and tangential separations
δ_n, δ_t	normal and tangential final crack opening widths
δ_{nc}, δ_{tc}	critical normal and tangential crack opening widths
λ_n, λ_t	initial slope indicators
σ_{max}, τ_{max}	normal and tangential cohesive strengths
T_n, T_t	normal and tangential cohesive tractions
m, n	non-dimensional exponents
α, β	shape parameters
Γ_n, Γ_t	normal and tangential energy constants
Ψ	cohesive potential function

Grain Material Parameters

v	Poisson's ratio
E	Young's modulus
m	strain rate sensitivity parameter
g_o	initial slip resistance
$\dot{\gamma}_o$	reference shear rate parameter
G_o	hardening rate parameter
g_s	saturation hardening
C	fourth-order elasticity tensor
μ	C_{44}
λ	C_{12}
η	$\frac{2C_{44}+C_{12}-C_{11}}{2}$
$\varphi_1, \phi, \varphi_2$	Euler angles

Miscellaneous

$\Delta_{cohesive}$	cohesive zone size
$\langle\bullet\rangle$	Macaulay bracket $\langle x\rangle = \begin{cases} 0, & x < 0 \\ x, & x \geq 0 \end{cases}$
a	crack dimension

Appendix II: References

Anderson, T. (2005). "Fracture Mechanics in Metals." *Fracture Mechanics: Fundamentals and Applications*. CRC Press, Boca Raton, FL, 249-250.

Balay, S., Gropp, W.D., Curfman McInnes, L., and Smith, B.F. (1997). "Efficient Management of Parallelism in Object Oriented Numerical Software Libraries." *Modern Software Tools in Scientific Computing* by Arge, E., Bruaset, A.M., and Langtangen, H.P. Birkhäuser Press, Boston, MA, 163-202.

Balay, S., Brown, J., Buschelman, K., Eijkhout, V., Gropp, W.D., Kaushik, D., Knepley, M.G., Curfman McInnes, L., Smith, B.F., and Zhang, H. (2010). *PETSc Users Manual*. ANL-95/11 - Revision 3.1, Argonne National Laboratory.

Balay, S., Brown, J., Buschelman, K., Gropp, W.D., Kaushik, D., Knepley, M.G., Curfman McInnes, L., Smith, B.F., and Zhang, H. (2011). "PETSc Web page." <http://www.mcs.anl.gov/petsc/> (Jan. 1, 2011).

Bozek, J.E., Hochhalter, J.D., Veilleux, M.G., Liu, M., Heber, G., Sintay, S.D., Rollett, A.D., Littlewood, D.J., Maniatty, A.M., Weiland, H.,Christ R.J. Jr., Payne, J., Welsh, G., Harlow, D,G., Wawrzynek, P.A., and Ingraffea, A.R. (2008). "A Geometric Approach to Modeling Microstructurally Small Fatigue Crack Formation- Part I: Probabilistic Simulation of Constituent Particle Cracking in AA7075-T651." *Modelling Simul. Mater. Sci. Eng.*, 16(6), 1-28.

Dodhia, K. (2002). "Simulation of crack initiation in aluminum alloys with inclusions." M.S. thesis, Cornell University, Ithaca, NY.

Gall, K., Horstemeyer, M., Degner, B., McDowell, D., and Fan, J. (2001). "On the driving force for fatigue crack formation from inclusions and voids in a cast A356 aluminum alloy." *Int. J. Fracture*, 108, 207-233.

Grosskreutz, J., and Shaw, G. (1969). "Critical mechanisms in the development of fatigue cracks in 2024-t4 aluminum." *Proc., 2nd International Conference on Fracture*, Chapman and Hall, London, England, 620-629.

Hochhalter, J. D., Littlewood, D. J., Christ, R. J., Veilleux, M. G., Bozek, J. E., Ingraffea, A. R., and Maniatty, A. M. (2010). "A geometric approach to modeling microstructurally small fatigue crack formation: II. Physically based modeling of microstructure-dependent slip localization and actuation of the crack nucleation mechanism in AA 7075-T651." *Modelling Simul. Mater. Sci. Eng.*, 18(4), 1-33.

Hochhalter, J.D. (2010). "Finite element simulations of fatigue crack stages in AA 7075-T651 Microstructure." Ph.D. thesis, Cornell University, Ithaca, NY.

Iesulauro, E. (2006). "Decohesion of grain boundaries in statistical representations of aluminum polycrystals." Ph.D. thesis, Cornell University, Ithaca, NY.

Matouš, K., and Maniatty, A. M. (2004). "Finite element formulation for modelling large deformations in elasto-viscoplastic polycrystals." *Int. J. Numer. Meth. Eng.*, 60(14), 2313-2333.

Needleman, A. (1987). "A continuum model for void nucleation by inclusion debonding." *J. Appl. Mech.*, 54(3), 525-531.

Needleman, A. (1990). "An analysis of tensile decohesion along an interface." *J. Mech. Phys. Solids*, Elsevier, 38(3), 289–324.

Park, K., Paulino, G. H., and Roesler, J. R. (2009). "A unified potential-based cohesive model of mixed-mode fracture." *J. Mech. Phys. Solids*, 57(6), 891-908.

Raj, R., and Ashby, M. (1975). "Intergranular fracture at elevated temperature." *Acta Metall. Mater.*, 23(6), 653-666.

Rice, J. R. (1968). “Mathematical Analysis in the Mechanics of Fracture.” *Fracture: An Advanced Treatise*, H. Liebowitz, ed., Academic Press, New York, NY, 191–311.

Tvergaard, V., and Hutchinson, J. (1992). “The relation between crack growth resistance and fracture process parameters in elastic-plastic solids.” *J. Mech. Phys. Solids*, 40(6), 1377-1397.

Veilleux, M. (2011). “Geometrically Explicit Finite Element Modeling of AA7075-T651 Microstructure with Fatigue Cracks.” Ph.D. thesis, Cornell University, Ithaca, NY.

Xu, X. P., and Needleman, A. (1993). “Void nucleation by inclusion debonding in a crystal matrix.” *Modelling Simul. Mater. Sci. Eng.*, 1(2), 111-132.